









Studying the impact of deuteron non-elastic breakup on $^{93}\text{Zr} + \text{d}$ reaction cross sections measured at 28 MeV/nucleon

Thomas Chillery ^{1,*}, Jongwon Hwang², Masanori Dozono³, Nobuaki Imai ¹, Shin'ichiro Michimasa ¹, Toshiyuki Sumikama⁴, Nobuyuki Chiga⁴, Shinsuke Ota⁵, Shinsuke Nakayama⁶, Deuk Soon Ahn⁴, Olga Beliuskina¹, Kazuya Chikaato⁷, Naoki Fukuda⁴, Seiya Hayakawa ¹, Eiji Ideguchi⁵, Kotaro Iribe⁸, Chihiro Iwamoto¹, Shoichiro Kawase ⁹, Keita Kawata³, Noritaka Kitamura¹, Kensuke Kusaka⁴, Shoichiro Masuoka¹, Hareru Miki¹⁰, Hiroari Miyatake¹¹, Daisuke Nagae ⁴, Ryo Nakajima¹, Keita Nakano⁹, Masao Ohtake⁴, Shunichiro Omika⁴, Hooi Jin Ong⁵, Hideaki Otsu ⁴, Hiroyoshi Sakurai⁴, Philipp Schrock¹, Hideki Shimizu¹, Yohei Shimizu⁴, Xiaohui Sun⁴, Daisuke Suzuki ⁴, Hiroshi Suzuki¹, Motonobu Takaki¹, Maya Takechi⁷, Hiroyuki Takeda⁴, Satoshi Takeuchi¹⁰, Takashi Teranishi⁸, Rieko Tsunoda¹, He Wang ⁴, Yukinobu Watanabe⁹, Yutaka X. Watanabe¹¹, Kathrin Wimmer ¹², Kentaro Yako¹, Hiroki Yamada¹⁰, Kazunari Yamada⁴, Hidetoshi Yamaguchi ¹, Lei Yang¹, Rikuto Yanagihara⁵, Yoshiyuki Yanagisawa⁴, Hiroya Yoshida⁸, Koichi Yoshida⁴, and Susumu Shimoura ¹

¹Center for Nuclear Study, the University of Tokyo, Wako, Saitama 351-0198, Japan

²Center for Exotic Nuclear Studies, Institute for Basic Science, Daejeon 34126, Republic of Korea

³Graduate School of Science, Kyoto University, Sakyo, Kyoto 606-8501, Japan

⁴RIKEN Nishina Center for Accelerator-Based Science, Wako, Saitama 351-0198, Japan

⁵Research Center for Nuclear Physics, Osaka University, Ibaraki, Osaka 567-0047, Japan

⁶Nuclear Data Center, Japan Atomic Energy Agency, Ibaraki 319-1195, Japan

⁷Department of Physics, Niigata University, Niigata, Niigata 950-2181, Japan

⁸Department of Physics, Kyushu University, 744 Motoooka, Nishi-ku, Fukuoka 819-0395, Japan

⁹Department of Advanced Energy Engineering Science, Kyushu University, Kasuga, Fukuoka 816-8580, Japan

¹⁰Department of Physics, Tokyo Institute of Technology, Meguro, Tokyo 158-8551, Japan

¹¹Wako Nuclear Science Center, IPNS, KEK, Wako, Saitama 351-0198, Japan

¹²GSI Helmholtzzentrum für Schwerionenforschung GmbH, Darmstadt 64291, Germany

* E-mail: t.chillery@cns.s.u-tokyo.ac.jp

Received July 14, 2023; Revised October 27, 2023; Accepted November 16, 2023; Published November 17, 2023

.....
The deuteron is a loosely bound system that can easily break up into its constituent proton and neutron whilst in the presence of Coulomb and nuclear fields. Previous experimental studies have shown that this breakup process has a significant impact on residual-nucleus production from deuteron bombardment in the high-energy range of 50–210 MeV/nucleon. However, there remains a lack of cross-section data at energies below 50 MeV/nucleon. The current study determined $^{93}\text{Zr} + \text{d}$ reaction cross sections under inverse kinematics at approximately 28 MeV/nucleon using the BigRIPS separator, OEDO beamline, and SHARAQ spectrometer. Cross sections from this research were compared with previous measurements and theoretical calculations. The experimental results show a large enhancement of the production cross sections of residual nuclei, especially those produced from a small number of particle emissions, compared to the proton-induced reaction data at simi-

lar bombarding energy. The DEURACS calculation, which quantitatively takes deuteron-breakup effects into account, reproduces the data well. As a long-lived fission product, ^{93}Zr remains a challenge for nuclear-waste disposal and treatment. This study's low-energy data may assist future consideration of nuclear-waste treatment facilities, where $^{93}\text{Zr} + d$ may feasibly transmute the waste into short-lived/stable nuclei.

.....
Subject Index D23, D50

Owing to the deuteron's weak binding energy (2.224 MeV) it is easily broken apart into its constituent proton and neutron by the Coulomb and nuclear fields of a target nucleus. Therefore, to completely understand the interactions between incident deuteron and target nucleus, consideration of the breakup processes is indispensable. During the entrance stage of deuteron-induced reactions, three different intermediate nuclei can be accessed by the absorption of either the deuteron or its constituent nucleons (neutron or proton). While the entire incident deuteron is possibly absorbed into the target nucleus by complete fusion (CF), nucleons from non-elastic breakup (NEB) of the deuteron may react with the target nucleus to produce highly excited intermediate nuclei. These nuclei may then undergo multiple particle and/or gamma-ray emissions until the exit channel is reached.

Theoretical models considering the CF, NEB, and elastic breakup (EB) mechanisms of deuteron reactions are under development including TALYS [1] and DEURACS [2], the outputs of which have shown close agreement with experimental cross-section trends up to 30 MeV/nucleon and 200 MeV/nucleon [3–5], respectively. In both codes, breakup processes of the incident deuteron are explicitly taken into account in the calculation of the production cross sections, and details of the calculation methods are found in Refs. [2,3]. The calculated total-production cross sections from DEURACS are given by the incoherent summation of the components of CF, NEB for the proton, and NEB for the neutron. This allows us to discuss the quantitative relationship between CF and NEB in the production of residual nuclei, which is difficult to distinguish experimentally. We emphasize, however, that the direct comparison between measured and calculated total-production cross sections is essential to cross-check theoretical outputs and understand the underlying mechanisms.

To simplify the comparison of CF and NEB, the NEB in this paper denotes the sum of the NEB contributions for the proton and neutron. DEURACS indicates that the NEB process enhances the production cross sections of residual nuclei produced from a small number of particle emissions at energies above 50 MeV/nucleon [6]. Recent experimental studies were performed for deuteron-induced reactions on ^{93}Zr , notably inverse-kinematics studies using radioactive ion (RI) beams across 50–210 MeV/nucleon [7–9]. However, additional cross-section data are needed at energies below 50 MeV/nucleon to further investigate the competition between CF and NEB, and benchmark current deuteron-breakup models at lower energies.

The present study determined the reaction cross sections of $^{93}\text{Zr} + d$ at 27.7 MeV/nucleon under inverse kinematics. The measurement was performed on the Optimized Energy Degrading Optics (OEDO) beamline [10] housed at the RIKEN RI Beam Factory (RIBF) [11] in Japan. This letter focuses on the analysis and results of this $^{93}\text{Zr} + d$ study, of which the main aims are to investigate the impact of deuteron breakup on the low-energy cross sections, and simultaneously contribute to low-energy nuclear data by extending the energy range covered by previous studies [7–9]. Our result may also assist transmutation facilities with treatment of

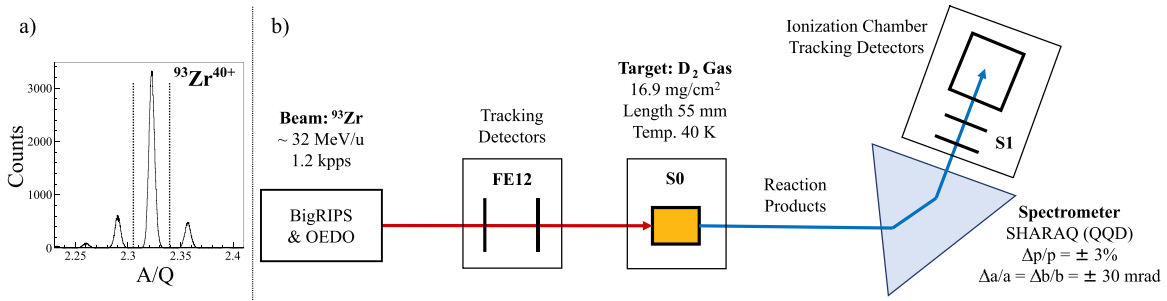


Fig. 1. (a) Beam mass-to-charge (A/Q) upstream of the target, where $^{93}\text{Zr}^{40+}$ is distinguished. (b) Diagram of the experimental setup around the S0 target. Details are provided in the text.

^{93}Zr ($T_{1/2} = 1.61$ Myr [12]), which remains a challenging long-lived fission product (LLFP) in the handling and disposal of radioactive nuclear waste [13–15].

The experiment was performed at the RIKEN RIBF in Japan. The Superconducting Ring Cyclotron accelerated into BigRIPS a primary beam of 345 MeV/nucleon ^{238}U , where it underwent in-flight fission by bombarding a ^9Be 5 mm thick target. The secondary beam fragments were transported through the BigRIPS separator, where the F1 momentum-acceptance slit was set to ± 3 mm. A 3.5 mm thick Al wedge-shaped (3.68 mrad) degrader was used to reduce the beam's kinetic energy from 140.0 MeV/nucleon to 32.0(4) MeV/nucleon. Diamond detectors [16] and parallel plate avalanche counter (PPAC) tracking detectors [17] measured the beam's time-of-flight (TOF) upstream of the target. The mass-to-charge (A/Q) of the beam, calculated from the central magnetic rigidity ($B\rho$) and TOF, is shown in Fig. 1(a). The $^{93}\text{Zr}^{40+}$ beam ions were clearly separated from contaminants (isotones of ^{93}Zr), and hereinafter “beam” refers only to ^{93}Zr . The beam was transported down to the OEDO beamline with intensity 1.2 kpps, where it bombarded a cryogenically cooled ($\simeq 40$ K) 16.9 mg/cm² thick, 55 mm long deuterium gas target [18] installed at focal plane S0. The gas target included Havar windows of approximately 10 μm thickness. The beamspot at S0 was focused using the OEDO radio-frequency deflector (RFD) and superconducting triplet quadrupole magnets, installed upstream of FE12. Details of the RFD's function are provided in Ref. [10]. The beamspot size at S0 in FWHM was 40 mm (12 mm) in X (Y). A diagram of the OEDO-SHARAQ beamline around the S0 target is shown in Fig. 1(b).

Reaction products from the D₂ target were collected and momentum-analyzed by the SHARAQ spectrometer, operated in QQD mode (further details may be found in Ref. [19]). Two PPAC tracking detectors were installed at each focal plane FE12 and S1, and were used to measure the position, timing, and $B\rho$ information of the ^{93}Zr beam and reaction products. The PPACs had position (timing) resolution of 0.8 mm (0.4 ns) in sigma. Towards the back of S1, a 30 pad ionization chamber (IC) with 750 mm active depth (1000 mm total depth from S1) was filled with 130 Torr CF₄ gas allowing successful stopping of the beam and products, thus measuring their Bragg curves for particle identification (PID). For each physics run, the SHARAQ D1 dipole magnet was set to one of five $B\rho$ settings $\Delta B\rho/B\rho_0 = -9.5\%$, -5.5% , -1.5% , $+2.5\%$, and $+6.0\%$ where 0% is the central beam trajectory ($B\rho_0 = 1.6210$ Tm). As such the charge-state distribution and acceptances of the beam and products were determined.

Measurements were performed with three different gas target settings at S0. The first setting used no gas target to check the beam condition at S1. In the second setting the gas target was installed with windows, but no gas. The third setting used the full gas target setup with

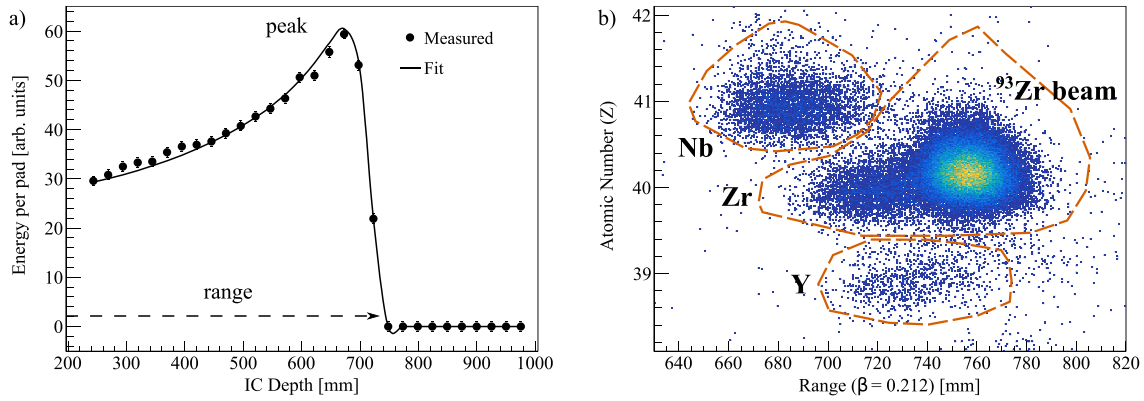


Fig. 2. (a) Sample Bragg peak collected by the ionization chamber at S1 using the measured energy deposited in each pad (markers) with complementary spline fitting (line). (b) Atomic number (Z) vs range of ions ($\beta = 0.212$) deposited in the IC at SHARAQ setting $\Delta B\rho/B\rho_0 = -1.5\%$. Dashed lines represent the 2D cuts applied to select each Z value.

flowing D_2 gas for the physics measurement. The target thickness was determined by measuring the beam energy with and without D_2 gas. The beam energy covered 25.1–30.3 MeV/nucleon through the gas target, with weighted average energy 27.7 MeV/nucleon.

The beam entering the gas target was counted from the TOF through the BigRIPS separator and OEDO beamline using diamond and PPAC anode timings, considering the target's active area from FE12 PPAC tracking information. Reaction products were identified at S1 using their $B\rho$, velocity (flight-path-length/TOF), Bragg peak energy, and range information. The $B\rho$ and flight-path-length through SHARAQ were extracted by fitting the tracking information from FE12 and S1 PPACs. The TOF was determined from the difference between S1 PPACs' anode timing and the timing extrapolated to S0 using FE12 PPACs' anode timing and position information. Using the $B\rho$ and velocity, A/Q was calculated as in Eq. (2) of Ref. [20]. The Bragg peak structure collected from the IC was fitted using a spline normalized to SRIM-2013 stopping-power data [21] to extract both the peak energy and range information event-by-event. A sample fit is shown in Fig. 2(a). The ion's mass number (A) is proportional to the range stopped in the chamber assuming that the energy per nucleon is the same as beam. Assigning the A value required careful consideration of the A/Q values of each locus; see Fig. 3(a). The ion's atomic number (Z) is proportional to the peak energy. To improve the Z -resolution, the fitted peak energy was corrected for high-order dependences on S1 x, y -positions due to the IC response. The atomic number vs IC depth of ions with $\beta = 0.212$, at setting $\Delta B\rho/B\rho_0 = -1.5\%$, is plotted in Fig. 2(b). The beam locus at approximate range 755 mm is significantly more intense than surrounding fragments due to its high intensity, and is stopped deeper in the IC than Zr fragments because of its larger incident kinetic energy. Beam contamination remained present in the $Z = 41$ region and, to resolve this, the Z -identification used 2D cuts on the atomic number vs range, shown by the dashed lines in Fig. 2(b), thus clearly separating each fragment, Nb, Zr, and Y.

The final PID was achieved using A vs A/Q gated on each Z locus. The fragments were counted for each $B\rho$ setting individually. A sample PID plot for setting $\Delta B\rho/B\rho_0 = -1.5\%$ is shown in Fig. 3(a), with its associated projection to A/Q in Fig. 3(b). Several loci are observed for the same isotope owing to the wide charge-state distributions encountered at this low energy, ~ 23.2 MeV/nucleon at S1. The full charge-state distribution was observed for

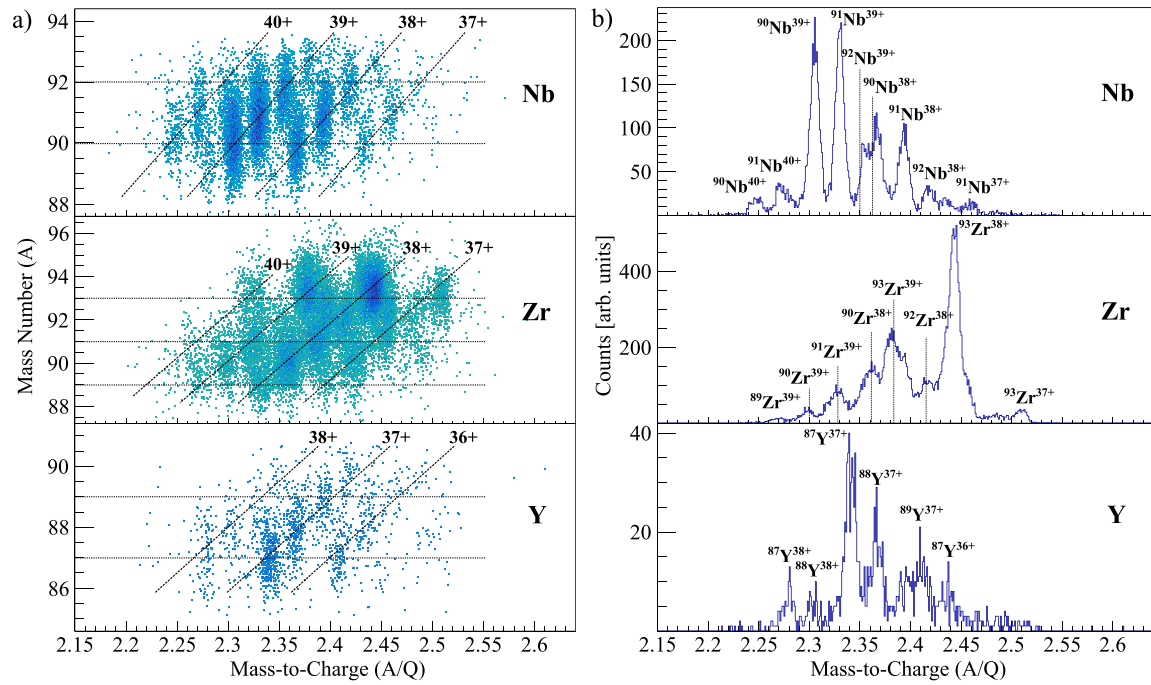


Fig. 3. Particle identification plots for SHARAQ setting $\Delta B\rho/B\rho_0 = -1.5\%$, gated on Z loci in Fig. 2(b). Dashed lines are to guide the eye. (a) Mass number (A) vs mass-to-charge (A/Q). (b) Projection of each PID plot to A/Q .

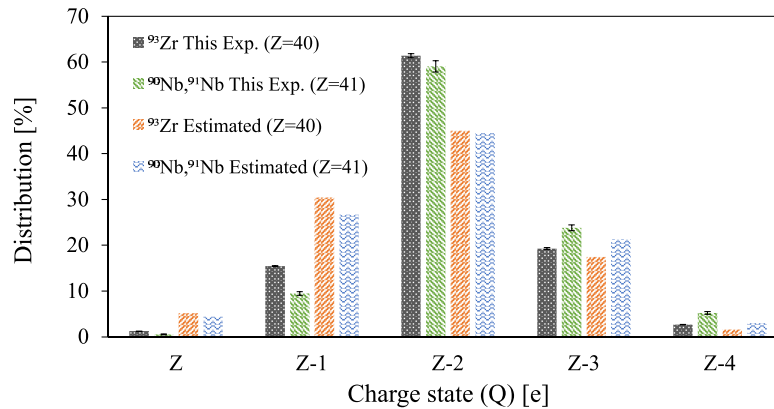


Fig. 4. Charge-state (Q) distributions of the 23.2 MeV/nucleon ^{93}Zr ($Z = 40$) beam and $^{90,91}\text{Nb}$ ($Z = 41$) fragments measured in this experiment. Estimated distributions are from the Leon method [22]. Statistical uncertainties to 1 sigma are included in the measured values.

the ^{93}Zr beam and $^{90,91}\text{Nb}$ reaction fragments by considering each $B\rho$ setting. The measured charge-state distributions of ^{93}Zr beam are plotted in Fig. 4. The weighted average of measured $^{90,91}\text{Nb}$ charge-state distributions is included in the histogram, and shows that the fragments have a distribution comparable to the beam. Predicted distributions from Leon's method [22] for both ^{93}Zr and $^{90,91}\text{Nb}$ are included, where it is noted that the measured distributions are sharper than predicted at the charge state of Z-2 for both Zr and Nb isotopes. The total counts for all charge states were extracted from a single dominant charge state based on the deduced distribution in the present data. When counting Zr and Y fragments their distributions were assumed to follow the ^{93}Zr (beam) distribution, whilst Nb isotopes used the weighted average of

the $^{90,91}\text{Nb}$ distributions. Using the beam distribution for the Y isotopes is deemed acceptable because of the similar ^{93}Zr (beam) and $^{91,90}\text{Nb}$ (fragment) distributions at Z-2.

The transmissions of beam and reaction fragments through SHARAQ were estimated from a Monte Carlo simulation code. The code used beam transport matrices calculated up to the third order by COSY Infinity v9.0 [23] to model the ion transport between S0 and S1. The starting condition at S0 was set using the measured beam condition from FE12 PPACs. SHARAQ's total acceptance was modeled by including the entrance and exit of the quadrupole and dipole magnets, the S1 PPAC active areas, and the window opening at the entrance to the IC. The simulation was normalized to the measured transmission of the ^{93}Zr beam. The average transmission through SHARAQ for both beam and fragments was approximately 89%.

The number of each identified isotope was counted from their respective locus in the PID (A vs A/Q). The cross section σ_d was then calculated from reaction yield Y as:

$$Y = \frac{N}{N_b N_Q T_{\text{SRQ}} H_{\text{LT}} \eta_{\text{S1}}}, \quad (1)$$

$$\sigma_d = \frac{(Y_{\text{phys}} - Y_{\text{back}})}{X_{\text{D}_2}}, \quad (2)$$

where N is the number of counted fragments for a dominant accepted charge state Q , N_b the number of beams bombarding the D_2 gas target, N_Q the fractional distribution of the isotope's charge state, T_{SRQ} the SHARAQ transmission, H_{LT} the live time of the measurement triggered at the S1 focal plane, and η_{S1} the total efficiency of the S1 delay-line single-mode PPACs ($\sim 99\%$). The background yield Y_{back} was similarly determined using the no-gas target runs and subtracted from the yield with the gas target, Y_{phys} . The areal number density of the target, X_{D_2} , was $5.04(28) \times 10^{21} \text{ atom} \cdot \text{cm}^{-2}$, where the error arises from the SRIM-2013 stopping powers (5%) and the measured energy loss (2.6%).

The isotopic trend of the present experimental cross sections is plotted in Fig. 5, along with previous data from deuteron and proton studies [7,9]. Comparing the deuteron data, the present data end at a higher mass limit because incident particles with a lower kinetic energy can remove fewer nucleons than those with a higher energy, thereby restricting the mass range in our data. Our low-energy data have distinctly higher production cross sections of Nb and Zr isotopes near ^{93}Zr compared to previous studies. This is because nuclei with similar masses to ^{93}Zr are most likely produced by particle emission from relatively less excited intermediate nuclei. The present deuteron data generally have higher production cross sections than the proton data at similar incident energy [9], because the deuteron's total-reaction cross section is larger than the proton's owing to the larger geometrical cross section.

A production cross section for ^{93}Zr was not measured in this study because such events cannot be distinguished from unreacted beam in the target. Considering the $^{93}\text{Zr} + d$ system around 30 MeV/nucleon, there are several energetically available exit channels. For any possible fragments that were not detected in our setup we conclude their production cross sections are below the statistical limit of this measurement, estimated from the lowest detected yield of identified isotopes to be approximately 10 mb. The statistical uncertainties on this measurement's cross sections are between 1.7 and 10.9% depending on counting statistics. The systematic uncertainty is 6.0% for $^{91,90}\text{Nb}$ and 7.1% for other fragments, arising from the stopping power of SRIM-2013 (5%); measured energy loss in the target (2.6%); SHARAQ transmission (2.1%); and, for isotopes except $^{91,90}\text{Nb}$, the charge-state distribution (3.8%). The systematic uncertainty from S1 PPAC total efficiency, 0.06%, is negligible.

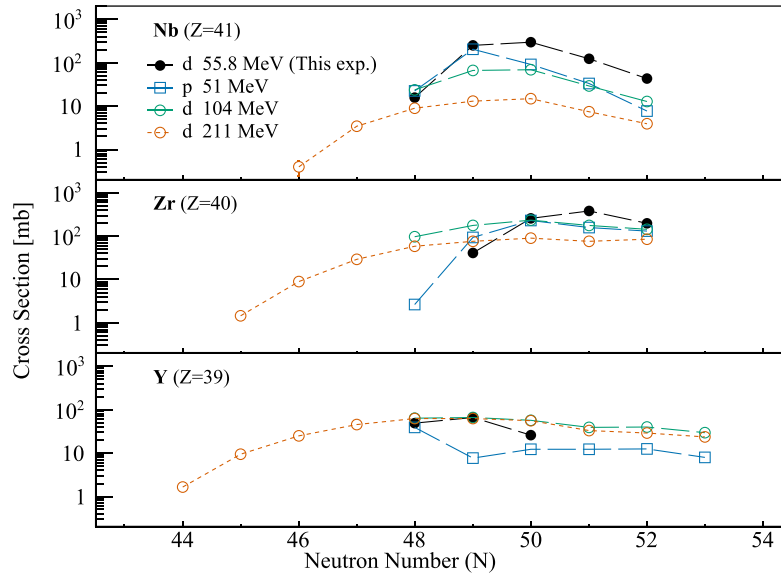


Fig. 5. Experimental cross sections for $^{93}\text{Zr} + \text{d/p}$ reactions as a function of neutron number (N). Legend energies are given in the laboratory frame (normal kinematics). Black circles are the present deuteron data at 55.8 MeV. Literature data are included for the 51 MeV proton [9] (blue hollow squares), 104 MeV deuteron [9] (green hollow circles), and 211 MeV deuteron [7] (orange hollow circles). Lines are to guide the eye.

Regarding our result's impact on the transmutation of ^{93}Zr waste, the increased Nb production cross sections may limit the effectiveness of low-energy deuteron-based treatment methods, simply because the half-lives of Nb isotopes can be exceedingly long, most importantly ^{92}Nb with $T_{1/2} = 34.7$ Myr [24]. During treatment at accelerator-based facilities the situation is likely more complex, as nuclei produced from the $^{93}\text{Zr} + \text{d}$ reactions may react with the deuteron beam themselves. Additionally, the deuteron-breakup and fusion-evaporation reactions produce light nuclei, e.g., neutrons, which may continue to transmute the surrounding target nuclei and significantly improve the transmutation yields [25]. To accurately assess the waste-treatment capabilities of deuteron-induced reactions, detailed simulations should be performed using an extensive reaction network around the ^{93}Zr region.

The measured cross sections will now be compared with the outputs of the DEURACS, CCONE [26], and TALYS calculations to discuss the impact of deuteron-breakup mechanisms. The $^{93}\text{Zr} + \text{d/p}$ reaction cross sections are plotted versus laboratory energy in Fig. 6. To simply compare the measured data with calculations, the energy axis represents the total incident energy of the deuteron or proton (normal kinematics). The present study's data are plotted at 55.8 MeV, where the hatched band represents the energy range covered in the D_2 target. Results from the literature are included at $(E_d, E_p) = (104, 51)$ MeV [9] and $(E_d, E_p) = (211, 106)$ MeV [7]. Total error bars are smaller than the marker sizes. The DEURACS curves use the model parameters as in Ref. [2], except with an improved description of the two-component exciton model for the calculation of the pre-equilibrium (PE) process. In the present calculation, the following effective transition matrix elements M^2 are used in the exciton model:

$$M^2 = \frac{A_p}{A_t^3} \left\{ 17 + \frac{4.2 \times 10^5}{\left(\frac{E}{nA_p} + 10.7\right)^3} \right\} [\text{MeV}]^2, \quad (3)$$

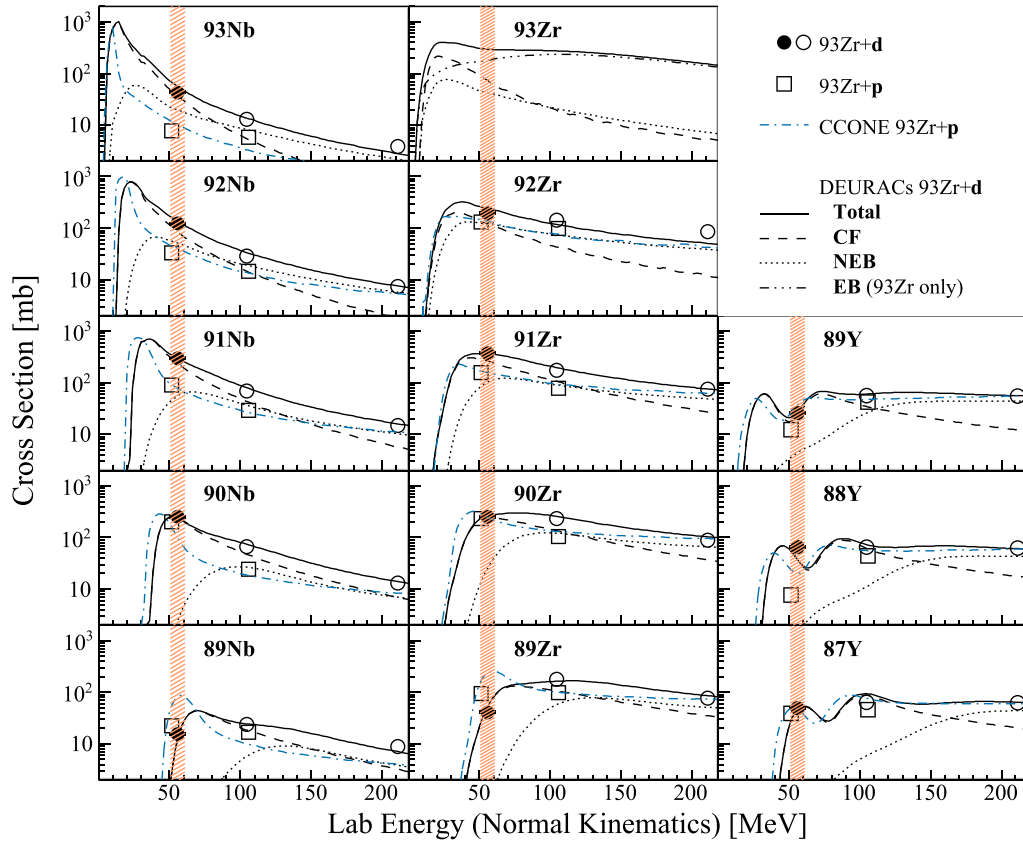


Fig. 6. Cross sections for $^{93}\text{Zr} + d/p$ reactions as a function of laboratory energy (normal kinematics). Each subplot is for a different produced isotope. The present data are plotted as solid circles at 55.8 MeV (27.7 MeV/nucleon), where the orange band width represents the energy covered in the D_2 gas target. Results from the literature for $^{93}\text{Zr} + d/p$ are included as hollow markers at other energies [7,9]. The total error bars are smaller than the marker sizes. Black lines (full, dashed, dotted, and triple-dot-dashed) are from DEURACS calculations of $^{93}\text{Zr} + d$. Blue dot-dashed lines are from CCONE calculations of $^{93}\text{Zr} + p$.

where A_p and A_t are the mass numbers of the projectile and target, respectively, E is the excitation energy, and n is the exciton number. The value of 17 MeV^2 in Eq. (3) was optimized from the recent analyses of residual-production cross sections of proton-induced reactions on LLFP targets [27]. In addition, the dependence on the projectile mass number A_p is newly introduced in M^2 according to the description of Eq. (172) in Ref. [1]. Solid lines represent the total $^{93}\text{Zr} + d$ production cross sections of each isotope from the DEURACS calculations. Dashed lines show the CF component from the deuteron and dotted lines show the summed NEB component from protons and neutrons arising from deuteron-breakup processes. Naturally, the neutron contribution to NEB for Nb isotopes is zero. The triple-dot-dashed curve for ^{93}Zr represents the EB component. The dot-dashed blue lines are the result of CCONE calculations of the $^{93}\text{Zr} + p$ reaction. The CCONE result is used to check whether the PE and compound-nucleus (CN) processes are correctly modeled for the proton and neutron reactions. Note that in DEURACS the subroutines of CCONE are used for the calculation of the PE and CN processes.

Our measurement and the previous higher-energy measurements are limited in that, because only heavy residues were detected, we cannot determine each reaction mechanism's

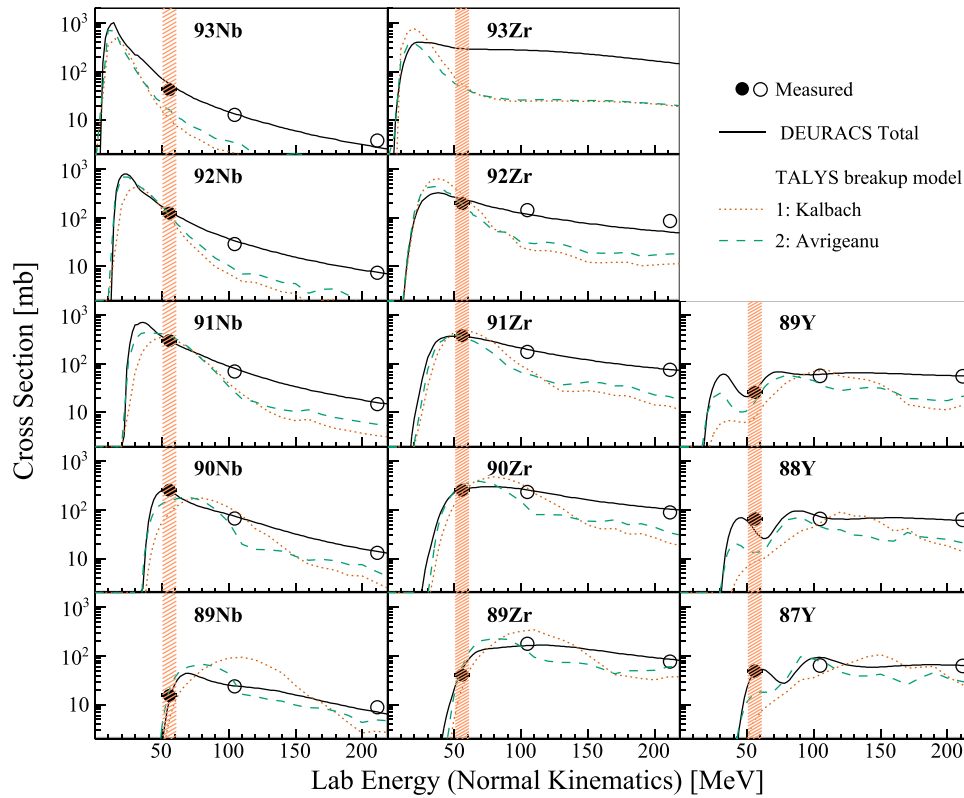


Fig. 7. Cross sections for $^{93}\text{Zr} + d$ reactions as a function of laboratory energy (normal kinematics). The measured data points and DEURACS total curve are the same as in Fig. 6. Dotted and dashed curves are from TALYS v1.96 calculations using the breakup models of Kalbach [28] and Avrigeanu [3], respectively.

contribution to the total-production cross sections from measured data alone. Instead, the measured data provide a strong constraint on the cross sections as calculated by DEURACS. At the deuteron energy of 55.8 MeV, the CF mechanism dominates over NEB during formation of the intermediate nuclei. Therefore in this experiment NEB is estimated to have a small contribution to the total-production cross sections compared to higher energies.

The measured cross sections are compared with outputs from both DEURACS and TALYS v1.96 in Fig. 7. In TALYS the breakup model was adjusted between Kalbach's model [28] and the recently implemented Avrigeanu model [3]. The predictive power of TALYS and DEURACS has been extensively discussed in Refs. [2,3]. The present production cross sections of Nb and Zr isotopes are quite well reproduced by TALYS, with the recent Avrigeanu model showing qualitative improvement over the Kalbach. The situation is different for Y-isotope production at our low energy, where the alpha emission channels for Y-isotope production are dominant. The TALYS alpha optical model potential was adjusted to use the Nolte model in an effort to best match the experimental data. However, the calculations still underestimate the Y-production cross sections up to a factor of 3 (11) with the Avrigeanu (Kalbach) breakup model. Evidently, continued efforts are required for theory to better describe our new results and improve models of deuteron-breakup mechanisms across the widest possible energy range.

In summary, we measured the $^{93}\text{Zr} + d$ production cross sections under inverse kinematics at weighted average energy 27.7 MeV/nucleon, the lowest energy to date. The low-energy beam

was successfully produced by the BigRIPS separator and OEDO beamline. Beam-like reaction products were identified downstream using the SHARAQ spectrometer, tracking detectors, and an ionization chamber. Comparison of empirical and theoretical cross sections over a wide energy range demonstrated that deuteron-breakup processes are essential to explain the measured data. In future, coincidence measurements that detect not only heavy residual particles but also evaporated light particles and γ -ray emissions would be helpful. The present data are indispensable for the transmutation of ^{93}Zr , which remains a big challenge for accelerator-driven transmutation systems. These systems may also benefit from similar measurements for other LLFPs.

Acknowledgements

We thank the RIKEN Nishina Center and the CNS, University of Tokyo accelerator staff for the excellent beam delivery. This research was funded by the ImPACT program of the Council for Science, Technology, and Innovation (Cabinet Office, Government of Japan), JSPS KAKENHI grants 19H01903 and 19H01914, and Ministry of Science and ICT, Korea grants IBS-R031-D1 and IBS-R031-Y2.

References

- [1] A. Koning, S. Hilaire, and S. Goreily, *Eur. Phys. J. A* **59**, 131 (2023).
- [2] S. Nakayama, N. Furutachi, O. Iwamoto, and Y. Watanabe, *Phys. Rev. C* **98**, 044606 (2018).
- [3] M. Avrigeanu, D. Rochman, A. Koning, U. Fischer, D. Leichtle, C. Costache, and V. Avrigeanu, *Eur. Phys. J. A* **58**, 3 (2022).
- [4] S. Nakayama, H. Kouno, Y. Watanabe, O. Iwamoto, and K. Ogata, *Phys. Rev. C*, **93**, 014618 (2016).
- [5] S. Nakayama, O. Iwamoto, Y. Watanabe, and K. Ogata, *J. Nucl. Sci. Technol.* **58**, 805 (2021).
- [6] H. Wang et al., *Commun. Phys.* **2**, 78 (2019).
- [7] S. Kawase et al., *Prog. Theor. Exp. Phys.* **2017**, 093D03 (2017).
- [8] S. Kawase, Y. Watanabe, K. Nakano, J. Suwa, H. Wang, N. Chiga, H. Otsu, H. Sakurai, S. Takeuchi, and T. Nakamura, *Proc. 2017 Symp. Nuclear Data (JAEA-Conf 2018-001)*, p 111 (2018).
- [9] K. Nakano et al., *EPJ Web Conf.* **239**, 20006 (2020).
- [10] S. Michimasa et al., *Prog. Theor. Exp. Phys.* **2019**, 043D01 (2019).
- [11] T. Kubo et al., *Prog. Theor. Exp. Phys.* **2012**, 03C003 (2012).
- [12] C. M. Baglin, *Nucl. Data Sheets* **112**, 1168 (2011).
- [13] P. Wydler and L. H. Baetsle, 6th Information Exchange Meeting on Actinide and Fission Product Partitioning and Transmutation, p. 31 (2001).
- [14] A. Hermanne, *J. Nucl. Sci. Technol.* **39**, 1202 (2002).
- [15] International Atomic Energy Agency, Status and Trends in Spent Fuel and Radioactive Waste Management, IAEA Nuclear Energy Series No. NW-T-1.14 (Rev. 1) (IAEA, Vienna, 2022).
- [16] S. Michimasa et al., *Nucl. Instrum. Methods Phys. Res. B* **317**, 710 (2013).
- [17] H. Kumagai, T. Ohnishi, N. Fukuda, H. Takeda, D. Kameda, N. Inabe, K. Yoshida, and T. Kubo, *Nucl. Instrum. Methods Phys. Res. B* **317**, 717 (2013).
- [18] H. Ryuto, M. Kunibu, T. Minemura, T. Motobayashi, K. Sagara, S. Shimoura, M. Tamaki, Y. Yanagisara, and Y. Yano, *Nucl. Instrum. Methods Phys. Res. A* **555**, 1 (2005).
- [19] S. Michimasa et al., *Nucl. Instrum. Methods Phys. Res. B* **540**, 194 (2023).
- [20] N. Fukuda, T. Kubo, T. Ohnishi, N. Inabe, H. Takeda, D. Kameda, and H. Suzuki, *Nucl. Instrum. Methods Phys. Res. B* **317**, 323 (2013).
- [21] J. F. Ziegler, SRIM - The Stopping Range of Ions in Matter(available at: <http://www.srim.org/>, date last accessed December 15, 2020).
- [22] A. Leon, et al., *At. Data Nucl. Data Tables* **69**, 217 (1998).
- [23] K. Makino, COSY Infinity(available at: https://www.bmtdynamics.org/index_cosy.htm, date last accessed April 10, 2023).
- [24] C. M. Baglin, *Nucl. Data Sheets* **113**, 2190 (2012).
- [25] M. T. Jin, S. Y. Xu, G. M. Yang, and J. Su, *Nucl. Sci. Tech.* **32**, 96 (2021).

- [26] O. Iwamoto, N. Iwamoto, S. Kunieda, F. Minato, and K. Shibata, Nucl. Data. Sheets **131**, 259 (2016).
- [27] S. Kunieda et al., J. Nucl. Sci. Technol. **56**, 1073 (2019).
- [28] C. Kalbach, Phys. Rev. C **95**, 014606 (2017).